Schweizerische Eidgenossenschaft
Confédération suisse
Confederazione Svizzera
Confederaziun svizra

Federal Department of the Environment, Transport,
Energy and Communications DETEC

Swiss Federal Office of Energy SFOE
Energy Research and Cleantech Division

REEL Demo – Romande Energie ELectric network in local balance Demonstrator

Deliverable: 2c Simulation and Experimental Validation of Linearized and Exact Convex AC OPF-based Real-time Controls on AIGLE Distribution Grid using PMU Measurements

Demo site: Aigle

Developed by
Rahul Gupta and Prof. Dr. Mario Paolone
Distributed Electrical Systems Laboratory, EPFL

[Lausanne, 20.05.2022]

1 Description of deliverable and goal

1.1 Executive summary

The objective of this deliverable is to validate a grid-aware real-time (RT) control algorithm for tracking a predefined power profile (dispatch plan) at the grid connection point (GCP) of a distribution network hosting heterogeneous multiple uncontrollable, and controllable energy resources. The RT control problem is formulated as Model Predictive Control (MPC) that computes the active and reactive power setpoints of a battery energy storage system (BESS) such that it tracks the dispatch plan at the GCP while obeying the constraints of the grid and the BESS.

The grid constraints are modeled by convex optimal power flow (OPF) models. Specifically, we consider two different OPF models: the first is the *Linearized Optimal Power Flow (L-OPF)* model that relies on the first-order Taylor series expansion of the nonlinear power flow equations to express the grid states (such as nodal voltages, lines currents and net grid losses) as linear functions of power injections. The second is the *Augmented Relaxed Optimal Power Flow (AR-OPF)*, which is an exact convex relaxation of the original non-linear non-convex OPF. The performances of the proposed RT controls with different grid models are compared against an a-posteriori non-approximated power flow. The comparison is assessed in terms of modeling error on the nodal voltages, lines currents and grid losses as well as the computation time.

Finally, the dominant grid model is used for experimental validation on an actual 24-node medium voltage (MV) distribution network in Aigle, Switzerland hosting uncontrollable 3.2 MWp distributed photovoltaic generation, 3.4 MVA hydro generations, and 2.8 MW base demand as uncontrollable resources and a 1.5 MVA/2.5 MWh BESS connected as the sole controllable resource. The grid situational awareness (i.e., time-synchronised measurements coupled to a real-time state estimator) is provided by 17 phasor measurement units installed at different locations in the grid.

1.2 Research question

Which OPF model is appropriate to accurately account for the grid constraints in a grid-aware real-time control scheme?

1.3 Novelty of the proposed solutions compared to the state-of-art

The main contributions of this work are listed below.

- Development of the grid-aware model predictive control of a BESS for achieving dispatch of a power distribution network hosting substantial amount of stochastic and non-controllable resources.

- Performance comparison of two different grid models in terms of accuracy and computation time.
- Validation of the dominant model in a full-scale real environment via the REeL demonstrator site in Aigle, Switzerland.

1.4 Methodology description

1.4.1 Control and Scheduling framework

We consider a distribution grid interfacing heterogeneous uncontrollable injections that is dispatched at its grid connection point (GCP) according to a pre-determined dispatch plan. The dispatch plan is tracked by controlling the grid-connected battery energy storage system (BESS) while respecting its own constraints along with those of the grid. It is formulated as two-stage framework. We refer to Fig. 1 that shows the dataflow during the day-ahead and real-time control stages. The two stages are described below.

- **Day-ahead scheduling:** the operator computes a dispatch plan for the next day based on the forecast of the stochastic generation and demand, the status of controllable resource (BESS in this case), and local grid constraints. The dispatch plan accounts for the uncertainties of the stochastic resources (modeled by scenarios) but also ensures that battery have a suitable level of flexibility to track the dispatch plan in real-time. We assume that the dispatch plan has a 5-minute resolution and is computed at 23.00 UTC the day before operations.
- **Real-time operations:** the BESS is controlled in real-time, so to compensate for power mismatches at the GCP between the realization and dispatch plan. The control problem is formulated as an MPC. It accounts for future uncertainties along the look-ahead horizon (5-minutes) and the grid's constraints. The MPC formulation aims to minimize the dispatch error over a 5-minute horizon actuated each 30 sec. Real-time operations start at 00.00 UTC and end at 23.59.59 UTC.

In the following, we present only on the real-time operation as it is the main focus of this deliverable. The dispatch plan is obtained from method described in [1].

1.5 Grid-aware Real-time operation

The real-time (RT) operation start at 00:00 local time. The objective of the RT controller is to achieve a fine tracking of the day-ahead dispatch plan while avoiding the saturation of the BESS SOC during the day's operation. Furthermore, at the end of the day, the framework has to restore a sufficient BESS SOC for reliably dispatching the feeder next day. Existing schemes in [2, 3] used a RT controller with an MPC look-ahead horizon of 5-minutes. However, this MPC is myopic to the uncertainties of the injections, eventually leading to BESS SOC saturation with a consequent loss of the tracking of the dispatch plan. We propose to avoid BESS SOC saturation by

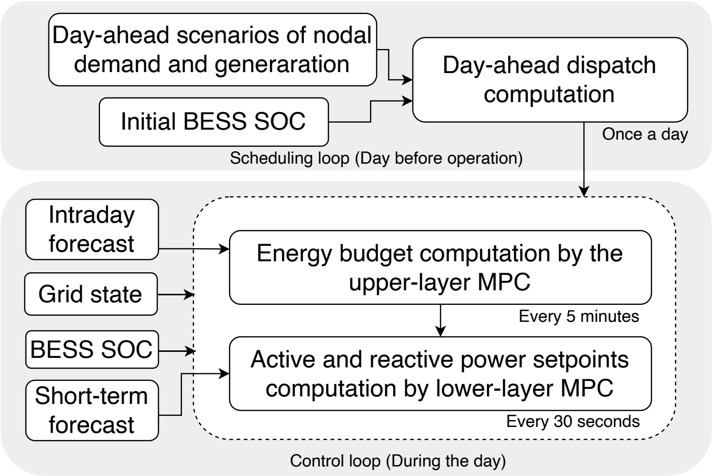

Figure 1: Schematic dataflow of the proposed scheduling and control framework.

adding a farsighted MPC layer imposing an SOC budget. This feature is enabled by the proposed two-layered MPC framework where the upper layer (farsighted) takes care of the SOC saturation of the BESS, whereas the lower layer (myopic) aims to fine-track the dispatch plan.
The real-time control objective is to track the day-ahead dispatch plan during the day of operation using a BESS. As stated earlier, the real-time control scheme comprises two layers operating at 5-minutes and 30 seconds time resolutions. The control problems of both layers are formulated as MPC and require forecasts of the nodal power injections. The *Upper layer* MPC uses forecasts of the nodal power injections at 5-minutes time resolution, whereas the *Lower layer* MPC uses forecasts at 30-seconds time resolution.

The control framework accounts for the grid constraints i.e., the constraints on the nodal voltages, lines and transformer capacities via a grid model. It is described as follows.

1.5.1 Grid-model

Accounting for the grid constraints makes the control problem non-convex as the power-flow equations are inherently non-linear and non-convex. This is widely referred to as the optimal power flow (OPF) problem. OPF problems are generally intractable and difficult to solve [4, 5]. Therefore, to increase their tractability several convexification approaches are proposed in the literature. They can be broadly categorised in following two types.

1. **Linearization:** this category of OPF convexification linearizes the non-linear power flow equations around a known operating point. The scheme relies on the first or multiple orders of Taylor's series expansion of the power flow equations. It uses sensitivity coefficients of the state variables (nodal voltages and lines currents) with respect to the control variables (nodal active and reactive power

injections). A typical example is proposed in [6].

2. **Relaxation:** In this case, suitable relaxations are applied such that the overall problem becomes a convex problem. An example is the adoption of the Semidefinite relaxation as the Second-Order-Cone-Program (SOCP) [7].

In this work, we implement linearized OPF model of [6] and relaxed OPF model of [7]. In the following, we describe above two methods.

Nomenclature: we refer to generic two-port equivalent $\Pi-$model of the network branches shown Fig. 2. As anticipated before, we consider a radial grid configuration. Let index 0 refer to the slack bus. The symbol $S^t_{0,k} = P^t_{0,k} + iQ^t_{0,k}$ refer to the apparent power at the slack. Buses other than the slack are denoted by $1, \dots, L$ and are in the set $\mathcal{L}$. The upstream and downstream buses to bus l are denoted by symbol $up(l)$ and l respectively. The symbol $\mathbf{H}$ refers to adjacency matrix as defined in [7]. Let k be the time index in the set $\mathcal{K} = [1, \dots, K]$. Let $S^t_{l,k} = P^t_{l,k} + iQ^t_{l,k}$ and $S^b_{l,k} = P^b_{l,k} + iQ^b_{l,k}$ be the complex power that is entering the line l from top and bottom respectively; and f_l be the square of the current in line l flowing through z_l (see Fig. 2). $z_l = r_l + ix_l$ and $2b_l$ be the longitudinal impedance and shunt capacitance of line l. z^*_l refer to complex conjugate of z_l. Let $v_{l,k}$ be the square of the voltage magnitude at bus l and v^{min} and v^{max} the squares of the minimum and maximum of nodal voltages. I^{max}_l is the square of maximum current limits of the line l. Let $s_{l,k} = p_{l,k} + iq_{l,k}$ be the power absorbed at bus l. Let $s^{bess}_{l,k} = p^{bess}_{l,k} + iq^{bess}_{l,k}$ be the injections from BESS. The uncontrollable injections from demand, PV and hydro generation are modeled by their forecasts denoted as $\hat{p}^{load}_{l,k}$, $\hat{p}^{pv}_{l,k}$ and $\hat{p}^{hydro}_{l,k}$ respectively. The nodal active and reactive injections are $p_{l,k} = p^{bess}_{l,k} + \hat{p}^{pv}_{l,k} + \hat{p}^{hydro}_{l,k} - \hat{p}^{load}_{l,k}$ and $q_{l,k} = -q^{bess}_{l,k} - \hat{q}^{load}_{l,k} - \hat{q}^{hydro}_{l,k}$, respectively.

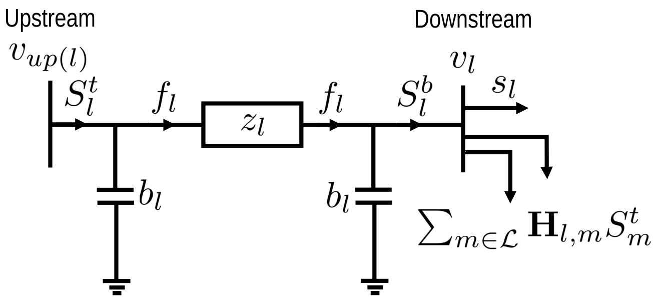

Figure 2: Illustration of the adopted nomenclature with respect to the generic two-port Π model of a transmission line.

Augemented Relaxed Optimal Power Flow (AR-OPF): According to [7], the AR-OPF constraints are composed of the SOCP relaxation of power flow equation (referred as relaxed (R)-OPF). The R-OPF equations are

$$S^t_{l,k} = s_{l,k} + \sum_{m\in\mathcal{L}} \mathbf{H}_{l,m} S^t_{m,k} + z_l\, f_{l,k} - j(v_{up(l),k} + v_{l,k}) b_l, \tag{1a}$$

$$S^b_{l,k} = s_{l,k} + \sum_{m\in\mathcal{L}} \mathbf{H}_{l,m} S^t_{m,k}, \quad \forall l \in \mathcal{L}, \forall k \in \mathcal{K}, \tag{1b}$$

$$v_{l,k} = v_{up(l),k} - 2\Re\Big(z^*_l \Big(S^t_{l,k} + j v_{up(l),k} b_l\Big)\Big) + |z_l|^2 f_{l,k}, \quad \forall l \in \mathcal{L}, \forall k \in \mathcal{K}, \tag{1c}$$

$$f_{l,k} \geq \frac{|S^t_{l,k} + j v_{up(l),k} b_l|^2}{v_{up(l),k}}, \quad \forall l \in \mathcal{L}, \quad \forall k \in \mathcal{K}, \tag{1d}$$

To guarantee the exactness of the OPF solution, the AR-OPF [7] introduces auxiliary variables to add security constraints on upper bounds of the nodal voltage and current magnitudes. It is done such that this upper bounds do not depend on original variable f rather an upper bound $\bar{f}$. Let symbols $\bar{f}, \hat{S}, \bar{S}$ are auxiliary variables for lines of the grid and $\bar{v}$ for the buses. The AR-OPF equations are defined as follows.

$$\hat{S}^t_{l,k} = s_{l,k} + \sum_{m\in\mathcal{L}} \mathbf{H}_{l,m} \hat{S}^t_{m,k} - j(\bar{v}_{up(l),k} + \bar{v}_{l,k}) b_l, \quad \forall l \in \mathcal{L}, \forall k \in \mathcal{K}, \tag{1e}$$

$$\hat{S}^b_{l,k} = s_{l,k} + \sum_{m\in\mathcal{L}} \mathbf{H}_{l,m} \hat{S}^t_{m,k}, \quad \forall l \in \mathcal{L}, \forall k \in \mathcal{K}, \tag{1f}$$

$$\bar{S}^t_{l,k} = s_{l,k} + \sum_{m\in\mathcal{L}} \mathbf{H}_{l,m} \bar{S}^t_{m,k} + z_l f_{l,k} - j(v_{up(l),k} + v_{l,k}) b_l, \quad \forall l \in \mathcal{L}, \forall k \in \mathcal{K}, \tag{1g}$$

$$\bar{S}^b_{l,k} = s_{l,k} + \sum_{m\in\mathcal{L}} \mathbf{H}_{l,m} \bar{S}^t_{m,k}, \quad \forall l \in \mathcal{L}, \forall k \in \mathcal{K}, \tag{1h}$$

$$\bar{v}_{l,k} = \bar{v}_{up(l),k} - 2\Re\Big(z^*_l (\hat{S}^t_{l,k} + j \bar{v}_{up(l),k} b_l)\Big), \quad \forall l \in \mathcal{L}, \forall k \in \mathcal{K}, \tag{1i}$$

$$\bar{f}_{l,k} v_{l,k} \geq |\max\{|\hat{Q}^b_{l,k} - j\bar{v}_{l,k} b_l|, |\bar{Q}^b_{l,k} - j v_{l,k} b_l|\}|^2 + |\max\{|\hat{P}^b_{l,k}|, |\bar{P}^b_{l,k}|\}|^2, \quad \forall l \in \mathcal{L}, \forall k \in \mathcal{K}, \tag{1j}$$

$$\begin{gathered}\bar{f}_{l,k} v_{up(l),k} \geq |\max\{|\hat{Q}^t_{l,k} + j\bar{v}_{up(l),k} b_l|, |\bar{Q}^t_{l,k} + j v_{up(l),k} b_l|\}|^2 + |\max\{|\hat{P}^t_{l,k}|, |\bar{P}^t_{l,k}|\}|^2, \\ \forall l \in \mathcal{L}, \forall k \in \mathcal{K},\end{gathered} \tag{1k}$$

$$I^{max}_l v_{up(l),k} \geq |\max\{|\hat{P}^t_{l,k}|, |\bar{P}^t_{l,k}|\}|^2 + |\max\{|\hat{Q}^t_{l,k}|, |\bar{Q}^t_{l,k}|\}|^2, \quad \forall l \in \mathcal{L}, \forall k \in \mathcal{K}, \tag{1l}$$

$$I^{max}_l v_{l,k} \geq |\max\{|\hat{P}^b_{l,k}|, |\bar{P}^b_{l,k}|\}|^2 + |\max\{|\hat{Q}^b_{l,k}|, |\bar{Q}^b_{l,k}|\}|^2, \quad \forall l \in \mathcal{L}, \forall k \in \mathcal{K}, \tag{1m}$$

$$v^{min} \leq v_{l,k}, \quad \bar{v}_{l,k} \leq v^{max}, \quad \forall l \in \mathcal{L}, \forall k \in \mathcal{K}, \tag{1n}$$

$$\bar{P}^t_{l,k} \leq P^{max}_l, \qquad \bar{Q}^t_{l,k} \leq Q^{max}_l, \quad \forall l \in \mathcal{L}, \forall k \in \mathcal{K}, \tag{1o}$$

Eq. 1e-(1f) express the lower bound on branch power flows at the sending and receiving ends of the line l, whereas the eq. (1g) and (1h) express the upper bound for power flows. Eq (1i) expresses the upper bound on the nodal voltages. These variables are then used in upper and lower bounds on the square of longitudinal current in eq. (1j) and (1k). Eq. (1l)- (1m) and eq. (1n) impose limits on the amapacities and nodal voltage respectively. Eq. (1o) expresses upper bound on the active and reactive power flows in line l where P^{max}_l/Q^{max}_l are bounds on active/reactive power flows in line l.

Linearized grid model: the linear grid model relies on the first-order Taylor's series expansion of the power flow equations. We use so-called sensitvity coefficients of the state-variables (i.e., the voltage and current sensitivity coefficients) to express them as linear functions of the control variables i.e. active and reactive power injections. Computing the sensitivity coefficients requires solving a system of linear equations as a function of the grid state and admittance matrix [8], whose solution is guaranteed to exist and be unique when the Jacobian of the load flow problem is locally invertible [9].

Nodal voltages and lines current magnitudes for all the nodes and lines are contained in vectors $\mathbf{v}_t \in \mathbb{R}^{|\mathcal{L}|}$ and $\mathbf{i}_k \in \mathbb{R}^{|\mathcal{L}|}$ at time index k, i,e., $\mathbf{v}_k = [v_{1,k};, \dots, v_{L,k}]$ and $\mathbf{i}_k = [i_{1,k};, \dots, i_{L,k}]$. The bold-typeface represents vectors. Symbols $\hat{\mathbf{p}}_k^{pv}, \hat{\mathbf{p}}_k^{load}$, $\hat{\mathbf{p}}_k^{hydro}$ and $\mathbf{q}^{\hat{pv}}{}_k, \hat{\mathbf{q}}_k^{load}$, $\hat{\mathbf{q}}_k^{hydro}$ collect aggregated active and reactive power injections of uncontrollable resources i.e. of PV, Load and Hydro plants of all the nodes, respectively. For example, $\hat{\mathbf{p}}_k^{pv}$ and $\hat{\mathbf{q}}_k^{pv}$ can be expanded as $\hat{\mathbf{p}}_k^{pv} = [\hat{p}_{1,k}^{pv}; \dots; \hat{p}_{L,k}^{pv}]$, $\mathbf{q}_k^{pv} = [q_{1,k}^{pv}; \dots; q_{L,k}^{pv}]$ (similarly for $\mathbf{p}_k^{load}$, $\mathbf{p}_k^{bess}, \mathbf{q}_k^{load}$, $\mathbf{q}_k^{bess}$). The injections from controllable BESS from all the nodes are contained in the vectors $\mathbf{p}_k^{bess}$ and $\mathbf{q}_k^{bess}$ for active and reactive powers respectively. In this setting, active and reactive nodal injections at time t read as:

$$\mathbf{p}_k = \mathbf{p}_k^{bess} + \hat{\mathbf{p}}_k^{pv} + \hat{\mathbf{p}}_k^{hydro} - \hat{\mathbf{p}}_k^{load} \qquad k \in \mathcal{K} \tag{2a}$$

$$\mathbf{q}_k = \mathbf{q}_k^{bess} + \hat{\mathbf{q}}_k^{pv} + \hat{\mathbf{q}}_k^{hydro} - \hat{\mathbf{q}}_k^{load} \qquad k \in \mathcal{K}. \tag{2b}$$

The linearized grid quantities as a function of the nodal injections and the grid states are

$$\mathbf{v}_k = \mathbf{A}_\mathbf{k}^\mathbf{v} \begin{bmatrix} \mathbf{p}_k \\ \mathbf{q}_k \end{bmatrix} + \mathbf{b}_k^\mathbf{v} \tag{2c}$$

$$\mathbf{i}_k = \mathbf{A}_\mathbf{k}^\mathbf{i} \begin{bmatrix} \mathbf{p}_k \\ \mathbf{q}_k \end{bmatrix} + \mathbf{b}_k^\mathbf{i} \tag{2d}$$

$$\begin{bmatrix} P_{0,k} \\ Q_{0,k} \end{bmatrix} = \mathbf{A}_k^{\text{gcp}} \begin{bmatrix} \mathbf{p}_k \\ \mathbf{q}_k \end{bmatrix} + \mathbf{b}_k^{\text{gcp}} \tag{2e}$$

where $\mathbf{A}_k^\mathbf{v} \in \mathbb{R}^{|\mathcal{N}| \times 2|\mathcal{N}|}$ and $\mathbf{b}_k^\mathbf{v} \in \mathbb{R}^{|\mathcal{N}|}$, $\mathbf{A}_k^\mathbf{i} \in \mathbb{R}^{|\mathcal{L}| \times 2|\mathcal{N}|}$ and $\mathbf{b}_k^\mathbf{i} \in \mathbb{R}^{|\mathcal{L}|}$, $\mathbf{A}_k^{\text{gcp}} \in \mathbb{R}^{2 \times 2|\mathcal{N}|}$ and $\mathbf{b}_k^{\text{gcp}} \in \mathbb{R}^2$ collect the sensitivity coefficients and known terms of the linear model as described in [6]. The grid constraints read as:

$$v^{min} \le v_{l,k} \le v^{min} \qquad l \in \mathcal{L}, k \in \mathcal{K} \tag{2f}$$

$$0 \le i_{l,k} \le I_{l,k}^{max} \qquad l \in \mathcal{L}, k \in \mathcal{K}. \tag{2g}$$

1.5.2 BESS model

As mentioned before, the BESS is controlled by an MPC to provide active and reactive power regulations to the grid while respecting the capability of the BESS power converter. Let P_l^{bess} and E_l^{bess} be the power and energy capacities of BESS connected at bus l. In a first approximation, the converter capability is represented by a circle ($(p_{l,k}^{bess})^2 + (q_{l,k}^{bess})^2 \leqslant {P_l^{bess}}^2$). However, such as representation is not true in practice as the power capability of the converter depends on both the AC and DC voltages of the converter. An example of capability curves with different combination of the AC and DC voltage are shown in Fig. 3a, and they can be represented by piece-wise-linear functions as follows.

$$\phi(v_t^{dc}, v_t^{ac}, p_l^B, q_l^B, P_l^{bess}) \leq 0. \tag{3a}$$

Here, v^{dc} is the DC bus voltage and v_t^{ac} is the magnitude of the direct sequence voltage on the AC side of the converter. They can be obtained from measurements or the BESS converter manufacturer.

Regarding the BESS losses by adding an equivalent resistance in the power flow equations as proposed in [10]. The approach integrates the equivalent resistance into the grid's admittance matrix by adding a extra line (l') for each BESS. It allows retaining the convexity of the AR-OPF problem without the need of any auxiliary variables. Fig. 3 shows the equivalent resistance with an ideal voltage source and series resistance (R_l^{bess}). Thanks to this model of the BESS losses (i.e., adding equivalent resistance into the grid's admittance matrix), the BESS state-of-energy (SOE) evolution with sampling time T_s is now expressed simply by

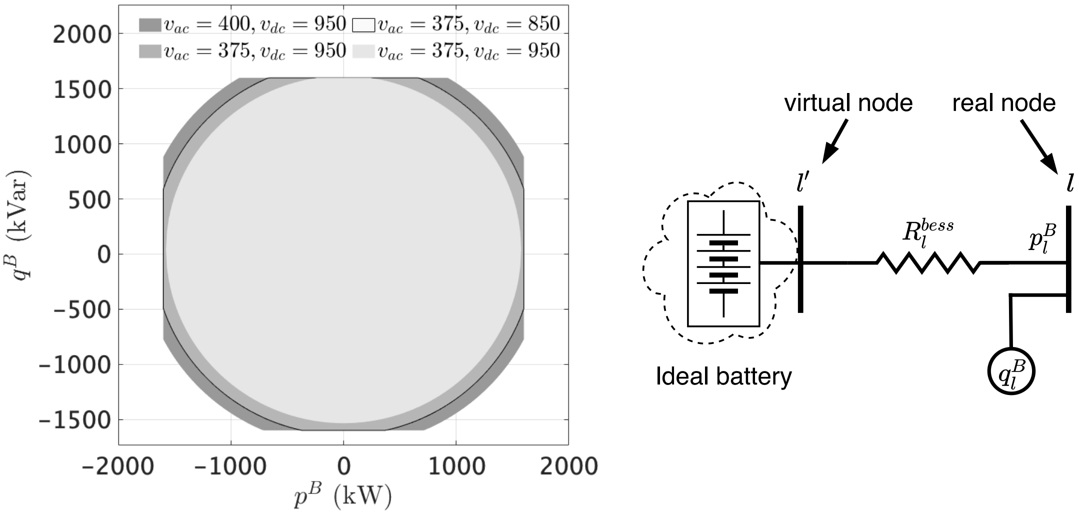

(a) (b)

Figure 3: (a) BESS converter capability function ϕ in eq.3a with AC and DC voltage. (b) Equivalent circuit diagram of BESS.

$$SOE_{l,k+1} = SOE_{l,k} + T_s p_{l,k}^{bess}, \qquad \forall l \in \mathcal{L}, \forall k \in \mathcal{K}. \tag{3b}$$

We constrain the SOE by safety margin of 0.1 per unit of the extremes saturation/depletion of the battery, namely:

$$0.1E_l^{bess} \leq SOE_{l,k} \leq 0.9E_l^{bess}, \qquad \forall l \in \mathcal{L}, \forall k \in \mathcal{K}, \tag{3c}$$

Furthermore, to account for the degradation of the BESS caused by its cycling, we include the following constraint that limits the active power by a pre-defined threshold:

$$\frac{T_s}{2 \times 3600} \left| p_{l,k}^{bess} \right| \leq N_e E_l^{bess}, \qquad \forall l \in \mathcal{L}, \forall k \in \mathcal{K} \tag{3d}$$

where N_e is the rated number of full cycles for the battery provided by the BESS manufacturer.

1.5.3 Model Predictive Control (MPC) Problem

As stated earlier, the real-time control scheme comprises two layers, both formulated as MPC but with different horizon lengths. The upper layer considers intra-day prosumption forecast along the whole day via subsequent shrinking horizon and computes successive BESS SOC trajectories. The lower layer considers forecast of 5-minutes interval with a shrinking horizon and computes power setpoints for the BESS while accounting for the SOC trajectory (provided by the upper layer) as hard constraint. This two-layered structure enables full visibility of the uncertainties during the real-time operation, therefore ensuring the BESS SOC to not saturate. Fig. 4 explains the sequence of operations during real-time operation per time step. The time intervals are divided into 5-minutes and 30-seconds slots corresponding to the sampling of upper and lower level MPCs.

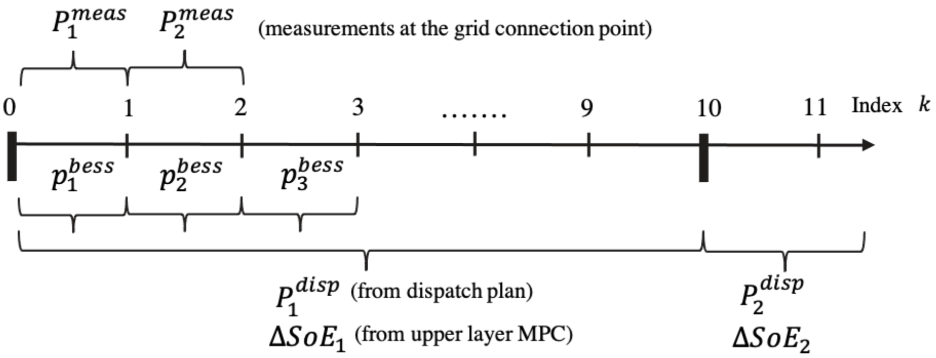

Figure 4: Sequence of decisions computed during real-time operations.

- The dispatch setpoint to track P_k^{disp} is retrieved from the dispatch plan profile with indices $k = 0, 1, \dots, N-1$ where $N = 288$ for 24 hours in a day. Intra-day forecasts $\hat{p}_{l,k}^{load}, \hat{q}_{l,k}^{load}, \hat{p}_{l,k}^{pv}, \hat{p}_{l,k}^{hydro}$, are updated.
- The upper layer MPC computes BESS energy budget $\Delta SOE_k,\ k = 0, 1, \dots, N-1$ every 5-minutes based on updated intra-day forecasts and current BESS SOE.

- The dispatch setpoint to track by the lower MPC is denoted by $\bar{P}^{disp}_{k} = P^{disp}_{\lfloor \frac{k}{10} \rfloor}$, where $\lfloor . \rfloor$ refers to the floor funtion. The first and the last 30-seconds index in current 5-minutes interval are denoted by $\underline{k}$ and $\bar{k}$ respectively, i.e., $\underline{k} = \lfloor \frac{k}{10} \rfloor \times 10$ and $\bar{k} = \underline{k} + 10 - 1$. The power measurements at the GCP denoted by $P^{meas}_{0,k}$ is obtained. Using $\bar{P}^{disp}_{k}, P^{meas}_{0,k}$ and ΔSOE_k, it computes BESS setpoints p^{bess}_{k} at time resolution of 30 seconds with indices $k = 0, 1, \dots, K-1 \in \mathcal{K}$ with $K = 2880$ for a 24 hours operation day.

Upper layer MPC: the objective is to minimize the tracking error between the dispatch plan P^{disp} and power at the GCP P^t_0. Note that P^t_0 is a dependent variable related to the uncontrollable power injections, the controllable BESS injections and the grid losses derived from AR-OPF (Eq.(1)). The decisions variables are the BESS active and reactive powers to compensate for the uncertainties in the nodal injections, the latter modeled by intraday point forecasts. The objective function to minimize is the weighted[1] sum of the tracking error for the whole day and grid losses[2]:

$$\begin{aligned} \widehat{p}^{bess}_{l} = \; & \underset{\forall S, v, s^B}{\text{arg min}} \; w_p \sum_{j=k}^{N} \| P^{disp}_{j} - P^{t}_{0,j} \|_2 + w_l \sum_{j=k}^{N} \sum_{l \in \mathcal{L}} r_l f_{lj} && \text{(4a)} \\ \text{subject to} \; & \text{grid constraints ((1) or (2))}, && \text{(4b)} \\ & \text{(3)}. && \text{(4c)} \end{aligned}$$

A bound on the final SOE such that it is restored to comfortable SOC by the day's operation is also added.

$$0.45 E^{bess}_{l} \leq SOE_{l,N} \leq 0.55 E^{bess}_{l}. \tag{4d}$$

The state of energy budget ΔSOE_l is computed using the first element of the BESS setpoint vector from upper-layer MPC:

$$\Delta \widehat{SOE}_l = \widehat{p}^{bess}_{l,1} \times \frac{300}{3600}. \tag{4e}$$

Lower layer MPC: the problem is formulated as an MPC and its objective is to minimize the energy error incurred over a 5 minutes horizon length with power setpoints actuated each 30 sec. The dispatch energy error at time k comprises of *(i)* uncovered energy error from time index $\underline{k}$ to $k-1$, $\hat{\epsilon}_k = \sum_{j=\underline{k}}^{k-1} (\bar{P}^{disp}_{j} - P^{meas}_{0,j})$ and *(ii)* the predicted error from k to $\bar{k}$ given as $\epsilon_k = \sum_{j=k}^{\bar{k}} (\bar{P}^{disp}_{j} - P^{t}_{0,j})$. The MPC goal is a multi-objective function comprised by the dispatch energy error incurred at the GCP

---

[1] The weights w_p, w_l and w_e may be derived from energy imbalance price in day-ahead electricity market.

[2] Grid losses are included to satisfy exactness conditions of the AR-OPF formulation as in [7]

(from current timestep to end of the 5-min period) and the grid losses:

$$\underset{\forall S, v, s^B}{\text{minimize}} \; w_e(\epsilon_k + \hat{\epsilon}_k) + w_l \sum_{k \in \mathcal{K}} \sum_{l \in \mathcal{L}} r_l f_{l,k} \tag{5a}$$

$$\text{subject to} \quad \text{grid constraints } ((1) \text{ or } (2)), \tag{5b}$$

$$(3). \tag{5c}$$

Additionally, the energy budget from the upper layer MPC are added as constraint imposed on the BESS SOE as:

$$SOE_{l,\bar{k}} \geq SOE_{l,\underline{k}} + \Delta\widehat{SOE}_l \quad \text{if} \quad \Delta\widehat{SOE}_l \geq 0, \tag{5d}$$

$$SOE_{l,\bar{k}} \leq SOE_{l,\underline{k}} + \Delta\widehat{SOE}_l \quad \text{if} \quad \Delta\widehat{SOE}_l \leq 0. \tag{5e}$$

The constraints in (5d) sets a threshold SOC to be attained by the end of current 5-minutes duration. It ensures that the BESS is used judiciously by the lower MPC to avoid its saturation and therefore restoring to comfortable SOC value by the end of the daily operation. Thanks to the convex reformulation of the AC power flow equations using AR-OPF, the control problems in (4) and (5) are convex and can be solved by standard solvers.

1.6 Experimental Validation

In the following, we present the experimental validation of the proposed real-time MPC algorithm. First, we compare the performance of the above two reported grid models in terms of their accuracy in modeling the grid constraints. Since the same experiment can not be repeated twice because of the uniqueness of weather conditions on each day, we perform this comparison via simulation. Finally, the dominant model is used for the experimental validation. The experimental setup is described below.

1.6.1 Experimental Setup

Medium voltage distribution network in Aigle, Switzerland: We validate the proposed control scheme on a real MV grid situated in Aigle, Switzerland, a mixed rural/urban system operated by Romande Energie,[3] one of the main Swiss DSOs. We consider a radial feeder composed by 24 nodes. The topology and locations of various connected resources are shown in Fig. 5a-5b. It is a three-phase 21 kV/20 MVA balanced (seen in the observations) system. The grid accommodates peak power consumption (at the feeder) of 4.3 MWp and 2.9 MWp during the winter and summer, respectively. It hosts aggregated PV generation capacity of 3.2 MWp including a single plant of 1.8 MWp. The grid also hosts distributed hydropower generation of 3.4 MVA allocated in 4 plants. The placement of these generations are shown in Fig. 5a. The grid is connected with a 1.5 MW/2.5 MWh BESS at node 11. Figure 5c shows

---

[3] https://www.romande-energie.ch/.

exterior and interior of the BESS. The cells are Lithium-Nickel-Manganese-Cobalt-Oxide (Li-NMCo) based and are rated for 4000 equivalent full cycles. It consists in 30 racks in parallel with 11 modules per rack in series (each module composed by 1p22s cell pack) connected to a four-quadrant power converter. The whole setup is installed in a temperature controlled container as shown in Fig. 5c. The technical specifications of the 1.5 MW/2.5 MWh BESS, including information of its cell technology as well as of its power conversion system (PCS) are included in the Table 1.

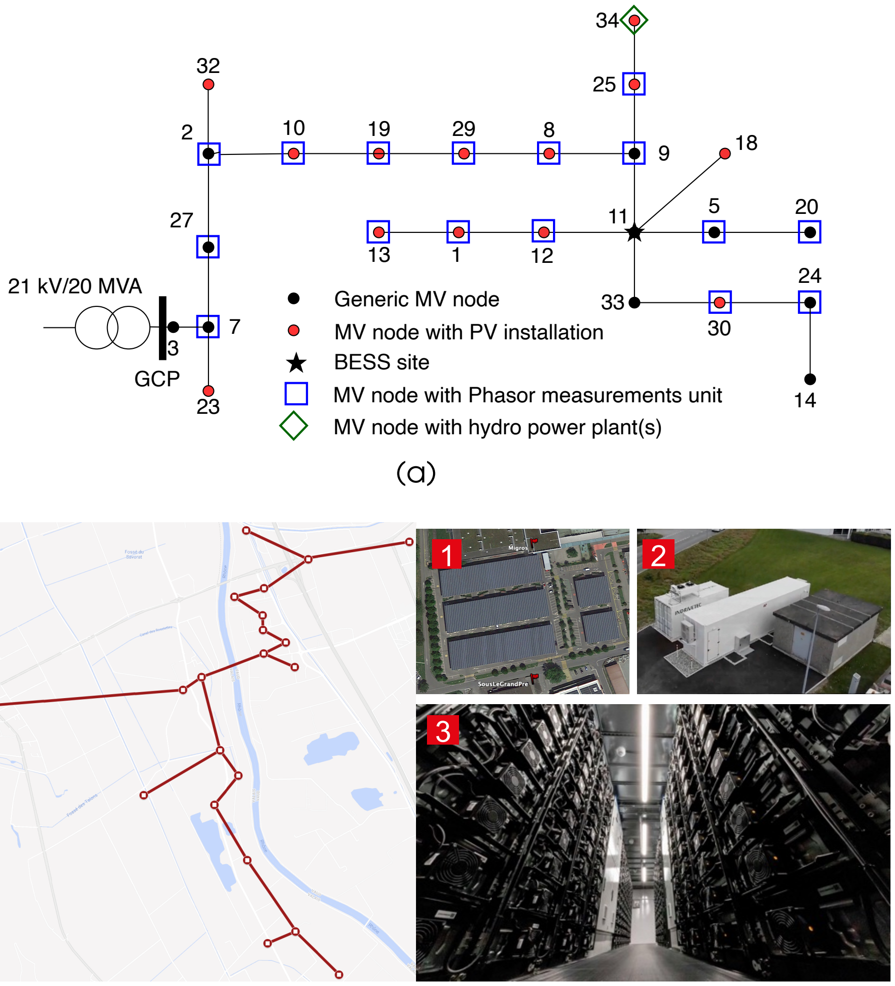

(a)

(b) (c)

Figure 5: (a) Topology with locations of the PMUs, PV plants, hydro-power plants, (b) Location of the substations and lines on the map, and (c) BESS and PV infrastructure: (1) Satellite view of the centralized PV plant of capacity 1.8 MWp, (2) battery container and (3) interior of the battery.

Phasor measurement units: the real-time MPC algorithm relies on the grid-awareness provided by a cluster of distributed metering units providing up-to-date relevant measurements such that they can be accounted as initial conditions in the MPC problem while optimizing the power set-points from the controllable resources and ensuring safe and secure operation of the grid. In this respect, the MV distribu-

Table 1: Technical specifications of the 1.5 MW/2.5 MWh BESS installed at the 21 kV MV grid of Romande Energie in Aigle, Vaud, Switzerland.

Parameter	**Value**
Nominal capacity	1.5 MVA/2.5 MWh
GCP Voltage	21 kV
DC bus voltage range	770-1000 V
PCS PQ controllability	4-quadrant operation
PCS efficiency	93 % for all the operating conditions
Total harmonic distortion	< 3 %
CSC operation mode	Compliant
VSC operation mode	Compliant
Cell technology	Lithium nickel manganese cobalt oxide (NMC)
Number of racks	30 in parallel
Number of modules per rack	11 in series
Cells configuration per module	1p22s
Total number of cells	7260
Cell nominal voltage	3.68 (limits 2.7 - 4.15 V)
Cell nominal capacity	94 Ah (343 Wh)
Battery cycle life	4000 equivalent cycle at 1C rate at 100 % DoD with 80 % of the initial storage capacity available at the end of life

tion grid is equipped with the state-of-the-art monitoring solution SynchroGuard[4] that provides real-time situational awareness of the grid. The setup contains 17 PMUs distributed across the grid, the locations are shown in Fig. 5a. The PMUs provide synchronised and time-tagged phasors which are sent to a central server using a telecom network (fiber optic or 4G). Fig 6a shows an example of the PMU and its components at a substation. A real-time state estimator (RTSE) accurately estimates nodal voltage and nodal/branch current and powers of the whole grid every 20 ms using only the PMU data. It is worth noting that the metering system is also a source of historical data that is used to obtain day-ahead scenarios, intra and short-term forecasts of the uncontrollable injections.

GHI and temperature measurement box: For modelling of the PV generation, we use historical data of GHI and air temperature from the same region where PV plants are located. So, we installed GHI and temperature sensing boxes (Meteobox) to measure the GHI, air- and PV-panel- temperatures. These meteoboxes are installed at three locations in the grid. They provide in real-time measurements with sampling of 500 ms (including communication latency). Fig 6b shows the installed meteobox at the site; each one consists of a pyranometer to sense the GHI, two temperature sensors, and a power supply. It also contains a modem which is used to stream the measured data using public 4G network to our data server. The meteobox code is implemented in NI compact RIO.

---

[4] https://zaphiro.ch/technology/.

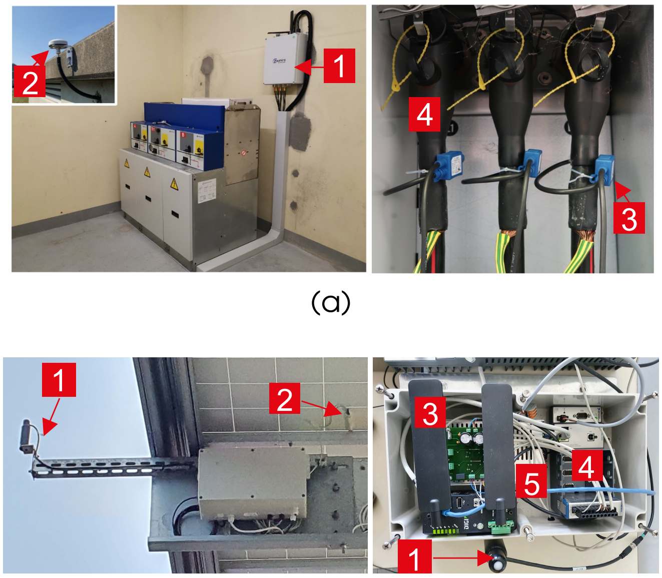

(a)

(b)

Figure 6: (a) PMU installation at a monitored substation, 1) Zaphiro PMU box 2) GPS antenna, (3) current sensor (4) cables and (b) GHI and temperature measurement box (Meteobox) at a PV plant: 1) pyranometer, (2) temperature sensor (3) antenna (4) power supply (5) NI Compact RIO.

1.6.2 Performance comparison of RT-MPC using Linearized *vs.* AR-OPF (Simulation)

To find the dominant grid model, we compare the performance of RT-MPC using the two grid models: (i) Linear OPF and ii) AR-OPF concerning their accuracy and computational speed. In the following, they are referred to as **L-OPF-MPC** and **AR-OPF-MPC** respectively. For sake of simplicity, the comparison is performed using **Single-layer MPC**, i.e. solving lower-layer MPC problem (eq. 5) but without SOE budget from upper layer MPC. The comparison is performed against the true quantities obtained by solving the non-linear load flow *a posteriori*. The results are compared looking at the root-mean-square-error (RMSE) and maximum absolute error (MAE) in the voltage, current magnitudes and grid losses. The comparisons are performed for a single day of experiments. Since the objective of this comparison is to establish the dominant grid model, the control performances are not shown. The control performances will be directly presented in the experimental results (Sec. 1.6.3)

Accuracy of the grid model: here, we compare the grid states i.e., nodal voltages, lines currents and losses computed by the L-OPF and AR-OPF model. They are compared against true values by solving non-linear AC power flow using the setpoint of BESS. Fig. 7a and 7b shows the nodal voltages using L-OPF and AR-OPF respectively. The plot in the upper panel shows the voltage computed by the OPF models whereas the lower panel shows error (in %) against true voltage. Similarly, Figs. 7c and 7d shows the lines current magnitudes (upper panel) and corresponding error (lower panel) using L-OPF and AR-OPF respectively. Finally, Figs 7e and 7f show the net grid losses (upper panel) and corresponding error (lower panel) with L-OPF and AR-OPF respectively. Fig. 7g shows the compare the CDF of the error in nodal voltages, lines currents and grid losses using L-OPF and AR-OPF. Table 2 presents the comparison of the two models in terms of maximum absolute error (MAE) and RMSE errors of the nodal voltages, lines currents and grid losses. From both the comparisons, it can be seen that AR-OPF model performs better on the lines current magnitude and grid losses by 87% and 90% on MAE. The error on the voltage magnitudes are slightly higher for AR-OPF however below than 5.5e-3% on maximum magnitude error.

Table 2: Error on the modeled voltage, currents and grid losses.

MPC	**Voltage error**		**Current error**		**Losses error**	
	RMSE (%)	MAE (%)	RMSE (%)	MAE (%)	RMSE (kW)	MAE (kW)
L-OPF-MPC	3.8e-5	2.2e-4	0.38	3.31	0.11	0.62
AR-OPF-MPC	2e-3	5.5e-3	0.14	0.45	0.04	0.06

Computational performance: we also compare the computation time using the two schemes. The comparison is shown in Table in terms of mean, maximum computation time. The MPC algorithms was simulated on a MacBook Pro with configuration of 2.7 GHz Quad Core Intel Core i7 and 16 GB Memory. Both the schemes achieve computation time below 30 seconds which is the time resolution of the MPC.

Table 3: Computation time

MPC	**Mean time (sec)**	**Max time (sec)**
L-OPF-MPC	1.29	2.46
AR-OPF-MPC	1.32	2.49

In summary, from above comparative analysis, the AR-OPF-MPC is more accurate concerning modeling of the lines current and grid losses. Thus, this model has been adopted for the experimental validation on the Aigle distribution network.

1.6.3 Experimental results

The dominant grid model from the last analysis, i.e., AR-OPF is used for the experimental validation on a real active distribution network. The experimental setup and the obtained results are described below. This section presents the experimental results obtained by dispatching the MV grid described in Sec. 1.6. We show results for two typical days representing different characteristics in terms of power injection patterns. On the first day, it imports net power into the grid, whereas on the second day, it exports net power during the middle of the day, thanks to generations from hydro and PV plants.

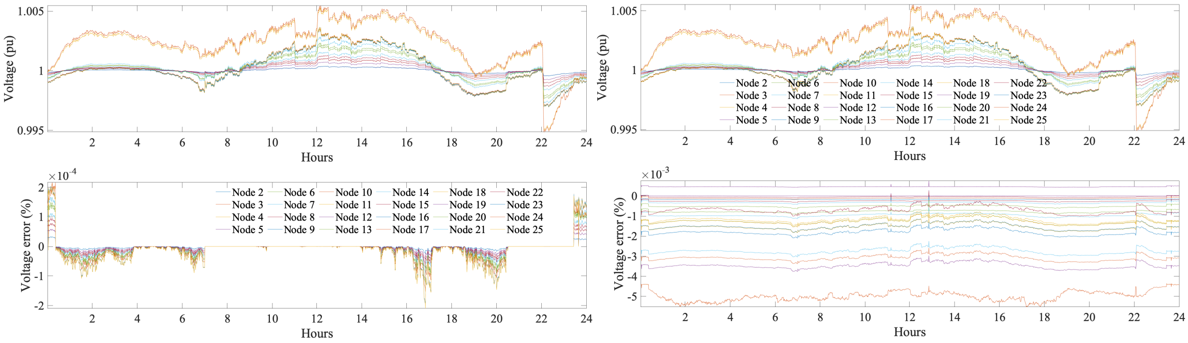

(a) Voltage computed using L-OPF. (b) Voltage computed using AR-OPF.

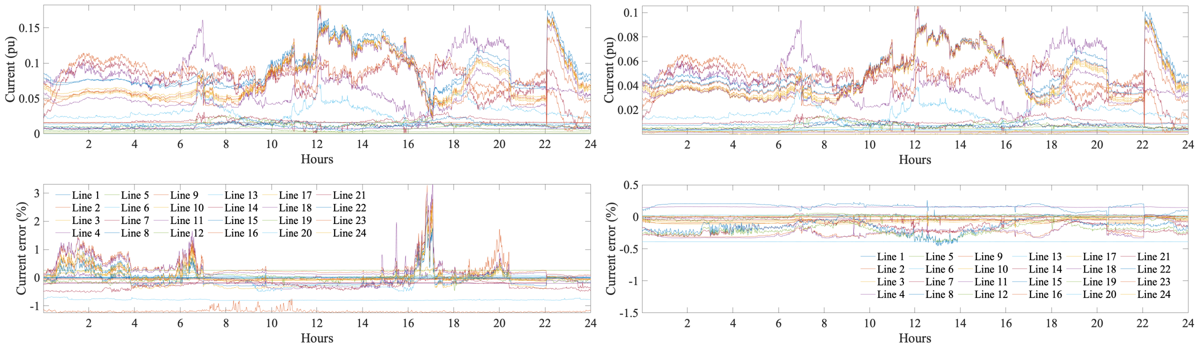

(c) Current computed using L-OPF. (d) Current computed using AR-OPF.

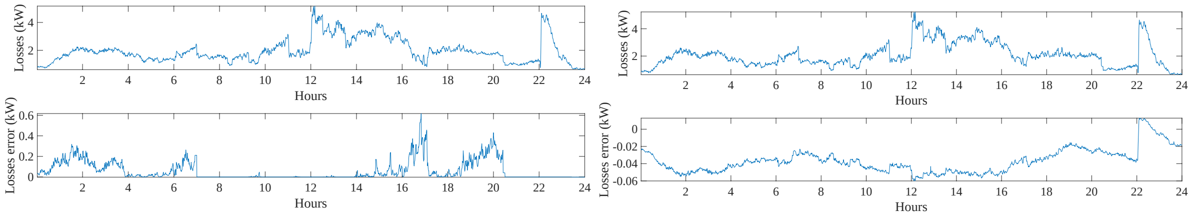

(e) Losses computed using L-OPF. (f) Losses computed using AR-OPF.

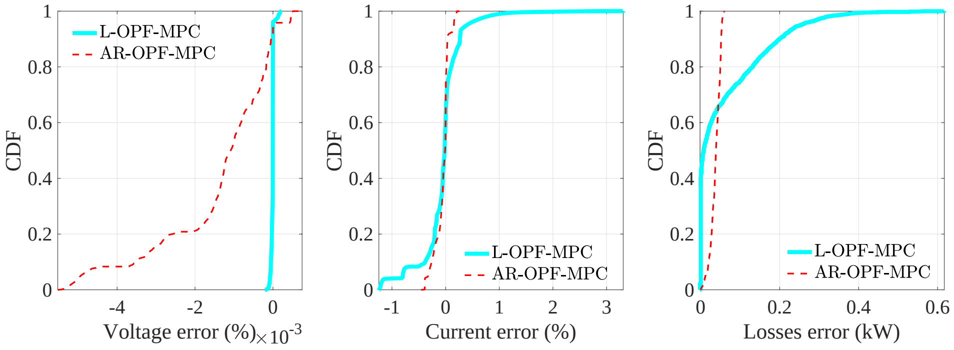

(g) CDF Errors of Voltage magnitude error (left), current magnitude error (middle) and grid losses (right).

Figure 7: Performance comparison of MPC using L-OPF and AR-OPF as grid models.

The control performance of the proposed two-layer MPC scheme is compared against other two cases: (i) **Without control**, where no compensation from BESS is performed, and (ii) a **Single-layer MPC**, solving single-layer MPC problem (eq. 5) but without SOE budget from upper layer MPC. Since the experiments were performed with the two-layer MPC, and the same experimental conditions can not be reproduced, we perform numerical simulations with single-layer MPC with same conditions as the day of operation for this comparison.

Day 1: Fig 8a shows the dispatch plan (in gray area), power at the GCP for different control schemes. Fig. 8b shows the SOC evolution with different control schemes. Fig 8c shows the plot of tracking error cumulative distribution function (CDF) as result of different real-time controls.

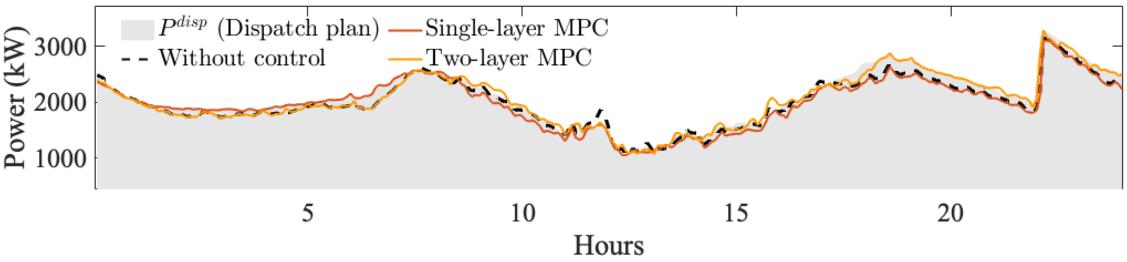

(a) GCP power tracking the dispatch plan with different control schemes.

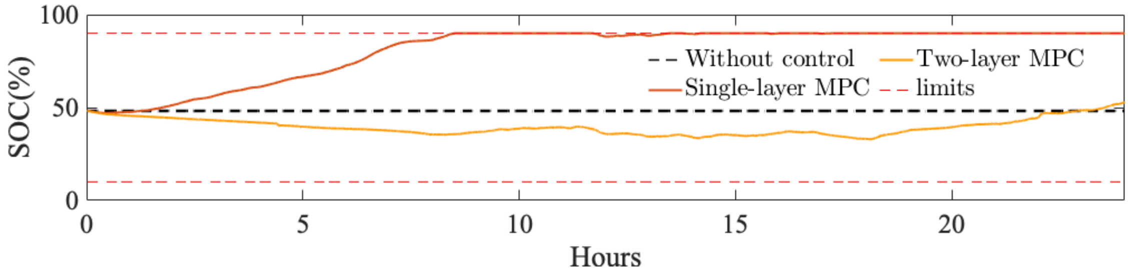

(b) SOC of the BESS with different control schemes.

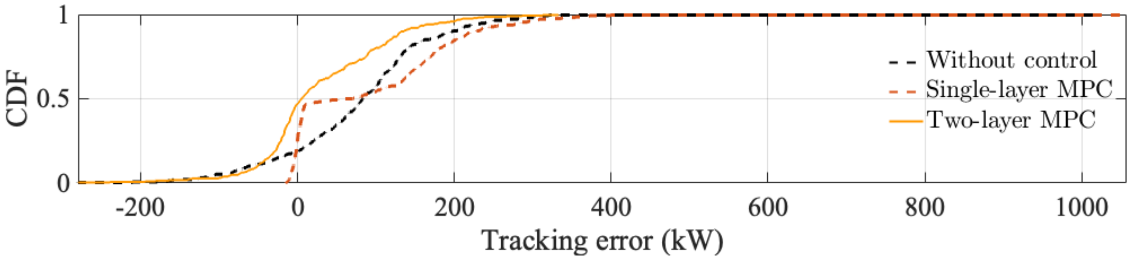

(c) CDF plot of the dispatch tracking error with different control schemes.

Figure 8: (a-c) Real-time operation for day 1 (01-Mar.-2022).

As it can be observed, the single-layer MPC lets the BESS saturate at around 8:00 hrs and it could not be used for the whole day; hence failing the dispatch. In contrast, the two-layer MPC ensures the BESS to never saturate, thanks to the energy budget constraints computed by the upper layer MPC. Also, by looking at the CDF plot of the tracking error in Fig. 8c, it is clear that two-layer MPC, on the one hand, achieves better tracking of the dispatch plan with a lower probability of high tracking error. On the other hand, it keeps the BESS SOC within a flexible range. Table 4 reports the maximum-absolute-error (MAE), net absolute-energy-error (AEE), root-mean-square-error (RMSE) of the dispatch error using different controls concluding that the control based on two-layer MPC performs the best. The two-layer MPC outperforms the single-layer MPC in RMSE by 40%, MAE by 67% and AEE by 35% respectively.

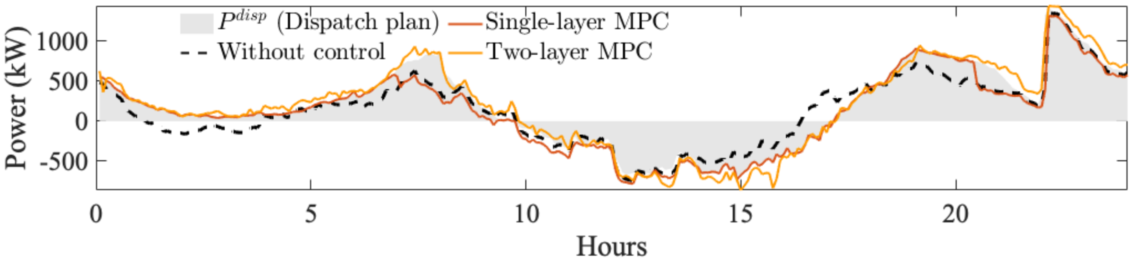

(a) GCP power tracking the dispatch plan with different control schemes.

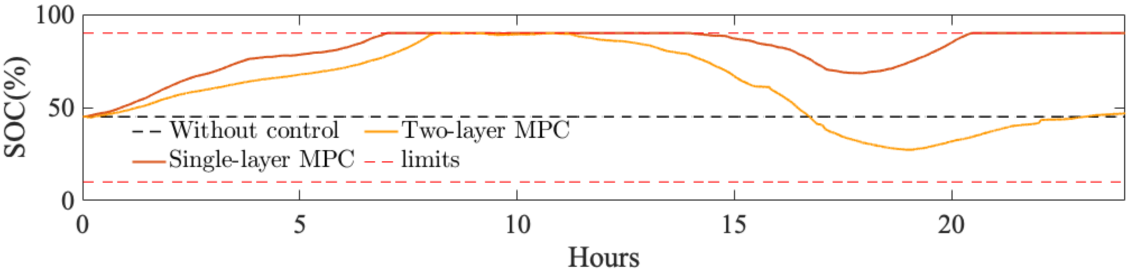

(b) SOC of the BESS with different control schemes.

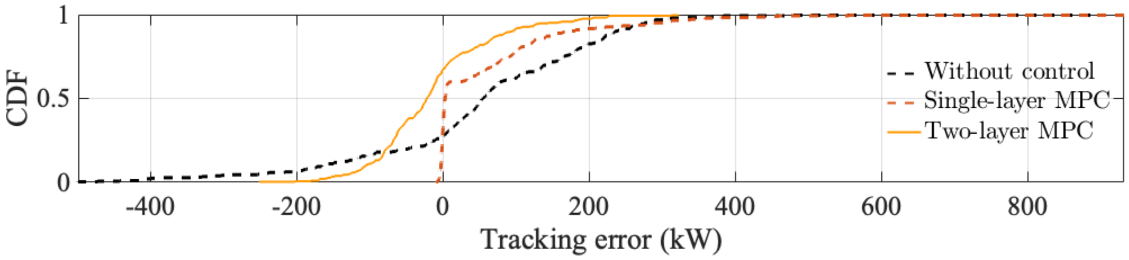

(c) CDF plot of the dispatch tracking error with different control schemes.

Figure 9: (a-c) Real-time operation.

Day 2: Fig. 9a shows the tracked dispatch plan using different control schemes. We show the BESS SOC, and the CDF of the dispatch tracking errors during the day in Fig. 9b and 9c respectively. Between 15.00 - 17.00, there is sudden drop in the PV generation (causing increased demand at the GCP) due to cloud passing resulting in increased mismatch between the dispatch plan and power at the GCP (without control). As observed, both the single- and two-layer MPCs achieves fine tracking of the dispatch plan for most of the day.

Table 4 reports the key metrics. It show slightly better performance for the single-layer MPC against the two-layer MPC, the latter restores the BESS to comfortable SOC of 45% (for the next day operation), whereas the single-layer MPC lets the BESS SOC to drop to 27%. The two-layer MPC sacrifices fine dispatch tracking from 19.00 till 23.59.30 to restore the BESS SOC from 20% to 45%. From the CDF plot in

Fig. 9, it can be observed that two-layer MPC achieves lower tracking error with high probability.

Table 4: Tracking error statistics with different control schemes.

MPC	**Day 1**			**Day 2**		
	RMSE (kW)	AEE (kWh)	MAE (kW)	RMSE (kW)	AEE (kWh)	MAE (kW)
None	137	2.5e3	1e3	176	3.2e3	896
Single-layer	148	2.3e3	1e3	124	1.5e3	932
Two-layer	89	1.5e3	332	85	1.5e3	322

2 Achievement of deliverable

2.1 Date

March 2022

2.2 Demonstration of the deliverable

This deliverable has been achieved through:

- the development of the control and scheduling framework
- accounting the grid constraints by two different optimal power flow models
- validation of the proposed methodologies in a full-scale real environment via the REeL demonstrator site in Aigle, Switzerland.

3 Impact

This deliverables represent the final outcome of a series of activities undertaken in the frame of ReEL. This involves the development of the OPF-based control methodology, a PMU-based real-time grid state monitoring and a short-term PV forecasting, all developed during the Phase I (2014-2016) of the SCCER-FURIES and patented, as well as the demonstration of those solutions in the real-grid of Aigle during the Phase II (2017-2020).

References

[1] A. Zecchino, R. K. Gupta, and M. Paolone, “Chapter(s) on the operation of the battery storage systems for grid control, feeder dispatching (RE Demo),” 2021.

[2] F. Sossan, E. Namor, R. Cherkaoui, and M. Paolone, “Achieving the dispatchability of distribution feeders through prosumers data driven forecasting and model predictive control of electrochemical storage,” *IEEE Trans. Sust. Energy*, vol. 7, no. 4, pp. 1762–1777, 2016.

[3] R. Gupta, F. Sossan, and M. Paolone, “Grid-aware distributed model predictive control of heterogeneous resources in a distribution network: Theory and experimental validation,” *IEEE Transactions on Energy Conversion*, vol. 36, no. 2, pp. 1392–1402, 2020.

[4] H. W. Dommel and W. F. Tinney, “Optimal power flow solutions,” *IEEE Trans. Power App. Syst.*, no. 10, pp. 1866–1876, 1968.

[5] M. Huneault and F. D. Galiana, “A survey of the optimal power flow literature,” *IEEE Trans. Power Syst.*, vol. 6, no. 2, pp. 762–770, 1991.

[6] R. Gupta, F. Sossan, and M. Paolone, “Performance Assessment of Linearized OPF-based Distributed Real-time Predictive Control,” in *IEEE PowerTech 2019*, Milan, Italy, Jun. 2019.

[7] M. Nick, R. Cherkaoui, J.-Y. Le Boudec, and M. Paolone, “An exact convex formulation of the optimal power flow in radial distribution networks including transverse components,” *IEEE Transactions on Automatic Control*, vol. 63, no. 3, pp. 682–697, 2017.

[8] K. Christakou *et al.*, “Efficient computation of sensitivity coefficients of node voltages and line currents in unbalanced radial electrical distribution networks,” *IEEE Trans. Smart Grid*, 2013.

[9] M. Paolone, J.-Y. Le Boudec, K. Christakou, and D.-C. Tomozei, *Advances in Power System Modelling, Control and Stability Analysis,*, 2016, ch. Optimal con-trol processes in active distribution networks, pp. 275–310.

[10] E. Stai *et al.*, “Dispatching stochastic heterogeneous resources accounting for grid and battery losses,” *IEEE Trans. on Smart Grid*, vol. 9, no. 6, pp. 6522–6539, 2018.